tvst

Article

Ultra-High Field Magnetic Resonance Imaging of the Retrobulbar Optic Nerve, Subarachnoid Space, and Optic Nerve Sheath in Emmetropic and Myopic Eyes

Bao N. Nguyen[1], Jon O. Cleary[2,3], Rebecca Glarin[2,4], Scott C. Kolbe[2,5], Bradford A. Moffat[2], Roger J. Ordidge[2], Bang V. Bui[1], and Allison M. McKendrick[1]

[1] Department of Optometry and Vision Sciences, The University of Melbourne, Parkville, Victoria, Australia
[2] Melbourne Brain Centre Imaging Unit, Department of Medicine and Radiology, The University of Melbourne, Parkville, Victoria, Australia
[3] Department of Radiology, Guy's and St. Thomas' NHS Foundation Trust, London, United Kingdom
[4] Department of Radiology, Royal Melbourne Hospital, Parkville, Victoria, Australia
[5] Department of Neuroscience, Central Clinical School, Monash University, Australia

Correspondence: Bao N. Nguyen, C/O Department of Optometry and Vision Sciences, The University of Melbourne, Parkville, Victoria 3010, Australia. e-mail: bnguyen@unimelb.edu.au

Received: February 10, 2020
Accepted: December 27, 2020
Published: February 9, 2021

Keywords: optic nerve; optic nerve sheath; subarachnoid space; ultra-high field; magnetic resonance imaging; 7 Tesla; myopia

Citation: Nguyen BN, Cleary JO, Glarin R, Kolbe SC, Moffat BA, Ordidge RJ, Bui BV, McKendrick AM. Ultra-high field magnetic resonance imaging of the retrobulbar optic nerve, subarachnoid space, and optic nerve sheath in emmetropic and myopic eyes. Trans Vis Sci Tech. 2021;10(2):8, https://doi.org/10.1167/tvst.10.2.8

Purpose: We aimed to image the optic nerve, subarachnoid space and optic nerve sheath in emmetropes and myopes ultra-high field (7-Tesla) magnetic resonance imaging (MRI). We targeted the retrobulbar distance of approximately 3 mm behind the eyeball, an area of clinical interest because of optic nerve sheath distensibility and pressure-related enlargement.

Methods: Eleven emmetropes (+0.75 to −0.50D, aged 20–41 years) and 10 myopes (−4.5 to −12D, aged 21–37 years) participated. Cross-sectional area of the optic nerve, subarachnoid space and optic nerve sheath at approximately 3 mm behind the eye were measured from two-dimensional T2-weighted coronal oblique MRI images obtained through the left optic nerve. Axial length of the left eye was measured from T2-weighted axial MRI images. In nine emmetropes and seven myopes, the optic nerve head was imaged with optical coherence tomography to compare retrobulbar and intraocular measures.

Results: Retrobulbar optic nerve, subarachnoid space and optic nerve sheath dimensions differed between myopes and emmetropes. Myopes tended to have smaller optic nerve and subarachnoid space. Longer MRI-derived axial length was associated with smaller optic nerve area ($P = 0.03$). Bruch's membrane opening area did not predict retrobulbar optic nerve area ($P = 0.48$).

Conclusions: This study demonstrates the feasibility of using 7-Tesla MRI to measure optic nerve, subarachnoid space, and optic nerve sheath dimensions behind the eye. In healthy adults, the retrobulbar optic nerve and subarachnoid space size are influenced by the degree of myopia.

Translational Relevance: ultra-high field MRI is a practical tool for assessing the morphometry of the optic nerve and surrounding anatomy behind the eye.

Introduction

The area behind the eye (approximately 3 mm posterior to the globe) is of significant clinical interest because at this retrobulbar distance, the optic nerve sheath is maximally distensible and susceptible to intracranial pressure–related enlargement.[1,2] After the optic nerve traverses the lamina cribrosa to exit the eye, it becomes myelinated and surrounded by a fluid-filled subarachnoid space, which is contiguous with intracranial cerebrospinal fluid. Surrounding the subarachnoid space is the optic nerve sheath, consisting of the dura mater meningeal membrane.[3,4] Changes in intracranial pressure can impact on the subarachnoid pressure around the optic nerve. Injecting fluid

into the subarachnoid space of postmortem eyes leads to increased diameter of optic nerve sheath, as demonstrated using transbulbar ultrasonography.[1,5,6] Similarly, increased intracranial pressure in vivo is correlated with optic nerve sheath diameter enlargement,[5,7–12] and vice versa,[13,14] which is visible clinically with ultrasonography and 1.5-Tesla (1.5T) and 3-Tesla (3T) magnetic resonance imaging (MRI).

One limitation of ultrasound and MRI studies to date is the exclusive reporting of optic nerve sheath diameter as a proxy for intracranial or subarachnoid pressure. However, increased optic nerve sheath diameter could possibly arise from increased optic nerve and/or subarachnoid space dimensions. Alternatively, an increase in one region (e.g., the subarachnoid space) could be associated with a concomitant decrease in another region (e.g., the optic nerve).[15,16] It is therefore useful to be able to image all three retrobulbar regions of interest (optic nerve, subarachnoid space, optic nerve sheath) simultaneously, which we were able to conduct here in healthy adults using MRI.

We chose to use MRI because ultrasonography tends to produce systematically smaller and more variable values of optic nerve sheath diameter than MRI.[17,18] Ultrasonography best resolves components that are perpendicular to the ultrasound beam,[17,18] which is non-ideal for our purpose given the oblique insertion of the optic nerve relative to the visual axis. On the other hand, MRI image planes can be freely acquired at any angle and personalized according to an individual's anatomy. Furthermore, the increase in MRI field strength to ultra-high field 7T has led to increased signal-to-noise ratio (SNR) and sub-millimeter spatial resolution of ophthalmic MRI.[19–21] Another technical advance we have exploited in this study is the use of a six-channel surface coil (instead of the standard head coil for MRI), with receiver elements placed close to the eye and the orbit to constrain scanning to this region of interest.[19–22] Each coil measures 36 mm wide and 71 mm high, providing sufficient radiofrequency depth penetration.[20]

Our first aim was to demonstrate feasibility of using 7T MRI and an eye-specific multichannel receiver coil to image the optic nerve, subarachnoid space, and optic nerve sheath at approximately 3 mm behind the eyeball. We chose to image healthy eyes with and without myopia because highly myopic eyes are at higher risk of glaucoma.[23] Although the reasons behind the increased risk of glaucoma in myopia are still unclear, a possible etiology is pressure-related optic nerve damage caused by changes in cerebrospinal fluid hydrodynamics, particularly where the subarachnoid space ends blindly at the posterior wall of the eyeball.[24] Given the range of histological and clinically observable changes that occur at the posterior eye of high myopes,[25,26] we hypothesized that increased myopia could impact on MRI-derived measures of retrobulbar anatomy. A secondary aim was to determine whether optical coherence tomography (OCT)–derived measures of optic nerve anatomy could predict MRI-derived retrobulbar dimensions, given that MRI is not always feasible in an ophthalmic clinical setting because of costs, claustrophobia, and other reasons for incompatibility.

Methods

Approval to conduct the study was granted by The University of Melbourne Human Research Ethics Committee (HREC ID no. 1646275), and the study protocol adhered to the tenets of the Declaration of Helsinki. Participants provided written informed consent and were deemed compatible for MRI by the radiographer prior to participation. Twenty-one healthy observers were prospectively recruited, comprising 11 emmetropes (+0.75 to −0.50D, aged 20–41 years, five females) and 10 myopes (−4.50 to −12.00D, aged 21–37 years, four females). The groups did not differ in age ($t_{19} = 0.60$, $P = 0.55$). All participants underwent an ophthalmic examination including subjective refraction, slit lamp examination, and ophthalmoscopy to ensure they met the study inclusion criteria: visual acuity of 6/7.5 or better in each eye, astigmatic correction <2.0D, intraocular pressure <21 mm Hg, normal anterior and posterior ocular health, no previous ocular trauma, surgery or orthokeratology, healthy maculae and optic discs, no pathological signs of high myopia (e.g., staphyloma, maculopathy), and no medications or systemic diseases known to affect visual function (e.g., diabetes).

Preparation and Setup for Magnetic Resonance Imaging (MRI)

MRI was performed at a single session at the Melbourne Brain Centre Imaging Unit at The University of Melbourne, using a 7T whole body scanner (Magnetom; Siemens Healthcare, Erlangen, Germany) and a dedicated six-channel transmit/receive eye coil (MRI.TOOLS GmbH, Berlin, Germany). The eye coil was placed as close as possible to the eyes, but without touching the skin, and stabilized using a custom-built plastic frame (Fig. 1A). Foam pads were placed between the ears and frame for comfort and to minimize head movement. Susceptibility artefact (i.e., image distortion and void in signal intensity created by the air-tissue interface, which is exacerbated at higher

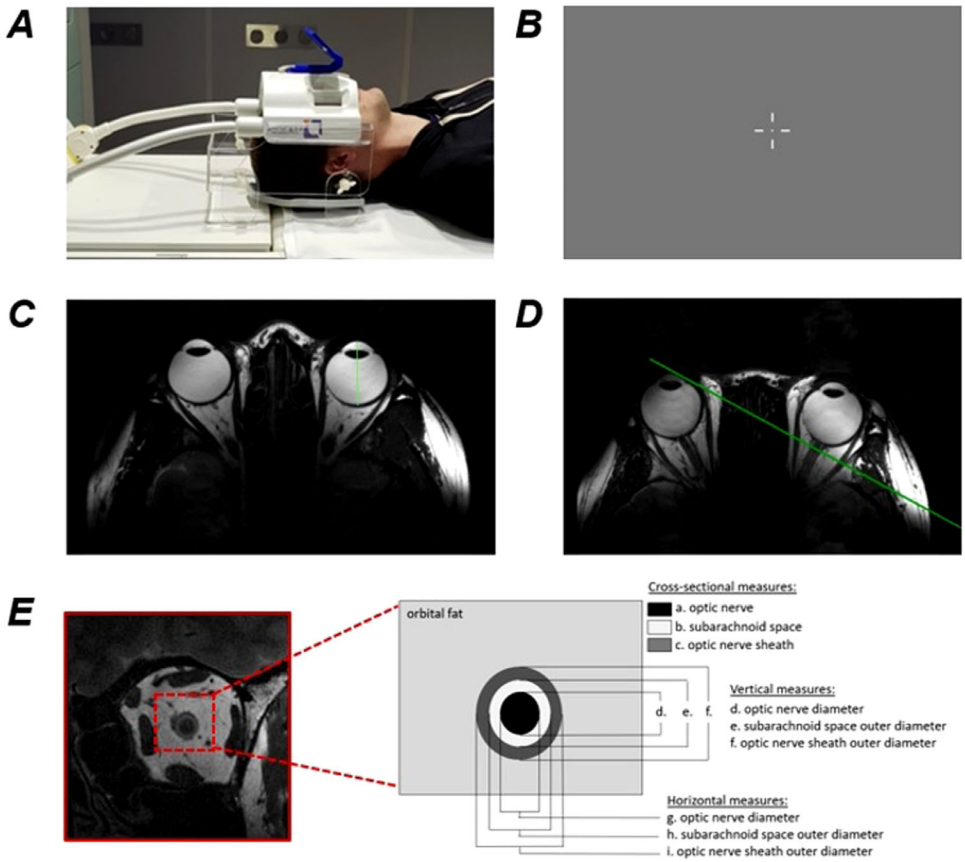

Figure 1. (**A**) Eye coil setup prior to entering the scanner. The eye coil was placed on a plastic frame for stability. Fixation was aided by an adjustable mirror (*blue*) connected to the eye coil at a 45° angle. (**B**) The fixation task consisted of four nonius lines pointing to a central target, which was customized in size (i.e., larger target for myopes, target size = minimum angle of resolution of visual acuity). (**C**) Example 2D T2-weighted axial image closest to eye equator to determine the MRI-derived axial length measurement, from a straight line manually placed between the posterior cornea and the vitreoretinal interface along the central axis, through the center of the lens and vitreous. (**D**) Example 2D T2-weighted axial image with superimposed scan plane (*green line*, in this case, 3 mm behind the eyeball), manually placed perpendicular to the insertion of the left eye optic nerve. (**E**) Example 2D T2-weighted coronal oblique image (enlarged and cropped), from which the optic nerve, subarachnoid space and optic nerve sheath were delineated manually. The main MRI-derived outcome measures of interest are schematized on the right: cross-sectional area of the (a) optic nerve, (b) subarachnoid space, and (c) optic nerve sheath (see Table 1 for cross-sectional measures); vertical outer diameters of the (d) optic nerve, (e) subarachnoid space, and (f) optic nerve sheath; and horizontal outer diameters of the (g) optic nerve, (h) subarachnoid space, and (i) optic nerve sheath (see Table 2 for diameter measures).

magnetic field strengths) and blinking was minimized by taping the left (imaged) eye shut.[21,27]

The right eye was used for fixation. Participants could view the fixation target (presented on a grey background at 142 cm distance) comfortably in primary gaze via a 45°-angled mirror attached to the eye coil (Fig. 1A). Corrective lenses could not be worn for the MRI scans (no prescription goggles or contact lenses). Previous ophthalmic MRI articles have raised the issue that imaging participants with impaired vision or high refractive errors would be challenging if a tiny, static fixation target is used.[19] Hence, we developed an interactive fixation task that ran continuously throughout the scan acquisition. Four white nonius lines remained on the screen to indicate the location of the central fixation target, which was either a red, blue, or white square that flashed on quasiperiodically (target presented for 150 ms duration, interval between each target presentation randomized to be any time between 1000 ms and 1500 ms). The size of the fixation target and thickness of the nonius lines were customized according to each participant's refractive error and uncorrected visual acuity (i.e., larger target for myopes, target size = minimum angle of resolution). Participants were asked to press the button when the fixation target was white and not to press the button when the target was red or blue. The randomized interstimulus interval for the fixation task was implemented to maintain attention. Participants were advised to blink normally throughout the scan acquisition.

Lubricating nonpreserved artificial tears (Theratears; Akorn Consumer Health, Ann Arbor, USA) were instilled for participants with self-reported dry eye. Each scan did not exceed three minutes, and participants were provided regular rest breaks in between scans. Participants tolerated the scans well and reported being comfortable throughout the session.

MRI Scans

An initial planning localizer scan (TR = 8.6 ms, TE = 4 ms, FOV = 300 mm, matrix = 384 pixels, resolution = 0.8 mm, slice thickness = 3 mm, scan time = 2′13″) was performed, followed by a 2D axial scan of both eyes (fast spin echo, T2-weighted, no fat suppression, TR = 2130 ms, TE = 73 ms, FOV = 150 mm, matrix = 384 pixels, resolution = 0.4 mm, number of slices = 12, slice thickness = 0.7 mm, scan time = 2′11″). The 2D axial scan served two purposes: (1) to enable measurement of MRI-derived axial length (Fig. 1C) and (2) to position the subsequent coronal oblique scans (T2-weighted, TR = 2000 ms, TE = 64 ms, FOV = 155 mm, matrix = 384 pixels, resolution = 0.4 mm, number of slices = 7, slice thickness = 0.7 mm, scan time = 2′40″) through the retrobulbar optic nerve.

Coronal oblique scan planes were positioned perpendicular to the optic nerve according to the initial axial planning scan, with placement of the first (of seven) slices intersecting approximately 3 mm posterior to the eyeball (see green line in Fig. 1D). Subsequent coronal oblique scans were placed adjacent to the first at regularly spaced intervals (20% or 1.4 mm overlap, which amounted to 5.6 mm increment spacing).

MRI Data Analysis

MRI-derived axial length of the left eye was first determined from the 2D T2-weighted axial images (Fig. 1C). The slice closest to the equator of the eye was chosen to determine axial length from the MRI images. Graders used the "length" tool to draw a single straight line between the cornea and vitreoretinal interface along the central axis through the center of the lens and vitreous (see green line in Fig. 1C). Corneal thickness was not included in the MRI-derived axial length measurement, because the posterior surface of the cornea was a more reliable anatomical landmark on visual inspection (i.e., higher contrast between the anterior chamber and posterior corneal surface, because closed lids can be indistinguishable from the anterior corneal surface[28]) and less likely to suffer susceptibility artefact compared to the anterior corneal surface.

To obtain our main retrobulbar cross-sectional area measures, one MRI image was chosen for analysis from the seven coronal oblique scans (i.e., the slice closest to 3 mm behind the eyeball). Six imaging graders (including one author) used the "closed polygon" tool in biomedical imaging software to manually delineate the optic nerve, subarachnoid space, and optic nerve sheath (see Fig. 1E, "cross-sectional areas"). The closed polygon tool connects adjacent points in a curvilinear fashion, hence, creating smoothed shapes. The cross-sectional area of each region of interest was automatically computed by the software according to the outer border. Smaller area measures were subtracted from larger area measures to calculate optic nerve sheath and subarachnoid space annular area (see Table 1).

For comparison to previous literature, the six imaging graders also manually marked the horizontal and vertical outer diameters (see Fig. 1E) of the optic nerve, subarachnoid space and optic nerve sheath (see Table 2). The lines were marked so that the horizontal and vertical lines intersected at the perceived center of the optic nerve (presumed ellipse). Horizontal and vertical diameters were averaged to determine the overall diameter of each structure, as is typically reported.[29] To calculate the thickness of the subarachnoid space annulus, the average optic nerve diameter was subtracted from the average outer diameter of the subarachnoid space and divided by two.[29] The same calculation was made for optic nerve sheath annulus thickness, that is, half the difference between the average outer diameters of the optic nerve sheath and subarachnoid space.

Ultrasound Biometry

In a subset of participants (10 emmetropes, seven myopes) who were available to attend an additional test session and consented to having eyedrops, axial length was measured using an A-scan ultrasound biometer (AL-100, Tomey, Nagoya, Japan) by contact method with one drop of 0.5% proxymetacaine hydrochloride in each eye. The biometer measures axial length as the distance from the anterior surface of the cornea to the internal limiting membrane (ILM) of the retina.

Optical Coherence Tomography

A secondary aim was to compare our retrobulbar MRI measures to optic nerve head parameters within the eye. Of the three layers of the intraocular optic nerve head, we chose to characterize Bruch's membrane opening (BMO) as the innermost opening

Table 1. MRI-Derived Retrobulbar Cross-Sectional Area Measurements (Mean ± Standard Deviation, Range) of the Optic Nerve, Subarachnoid Space and Optic Nerve Sheath Averaged From Six Graders[a]

	Emmetropes (n = 10)	Myopes (n = 9)	All (n = 19)	Intraclass Correlation Coefficient (95% CI)
Optic nerve area (mm^2)	8.8 ± 1.6 (6.5–11.5)	6.9 ± 2.7 (3.1–12.1)	7.9 ± 2.3 (3.1–12.1)	0.97 (0.95–0.99)
Subarachnoid space annular area (mm^2)	11.5 ± 3.1 (5.2–16.5)	9.0 ± 2.1 (5.7–12.1)	10.3 ± 2.9 (5.2–16.5)	0.96 (0.93–0.98)
Optic nerve sheath annular area (mm^2)	10.0 ± 2.0 (5.5–12.4)	12.0 ± 3.8 (7.7–18.6)	10.9 ± 3.1 (5.5–18.6)	0.95 (0.91–0.98)
Total optic nerve sheath complex area (mm^2)	30.3 ± 5.5 (18.1–37.8)	28.0 ± 7.1 (18.1–40.0)	29.2 ± 6.3 (18.1–40.0)	0.99 (0.97–0.99)

[a]Intraclass correlation coefficients (ICC) and their 95% confidence intervals are given.

Table 2. MRI-Derived Retrobulbar Outer Diameter Measurements (Mean ± Standard Deviation, Range) of the Optic Nerve, Subarachnoid Space, and Optic Nerve Sheath Averaged From Six Graders[a]

	Emmetropes (n = 10)	Myopes (n = 9)	All (n = 19)	Intraclass Correlation Coefficient (95% CI)
Optic nerve vertical diameter (mm)	3.5 ± 0.4 (2.8–4.1)	3.1 ± 0.8 (1.9–4.7)	3.3 ± 0.6 (1.9–4.7)	0.97 (0.94–0.99)
Optic nerve horizontal diameter (mm)	3.2 ± 0.3 (2.8–3.9)	2.8 ± 0.5 (1.9–3.3)	3.0 ± 0.4 (1.9–3.9)	0.94 (0.89–0.98)
Subarachnoid space vertical outer diameter (mm)	5.2 ± 0.6 (4.0–6.0)	4.6 ± 0.9 (3.4–6.4)	4.9 ± 0.8 (3.4–6.4)	0.98 (0.95–0.99)
Subarachnoid space horizontal outer diameter (mm)	4.9 ± 0.5 (3.9–5.6)	4.4 ± 0.5 (3.3–4.9)	4.7 ± 0.6 (3.3–5.6)	0.97 (0.93–0.99)
Optic nerve sheath vertical outer diameter (mm)	6.2 ± 0.6 (4.9–7.1)	6.2 ± 1.2 (4.8–8.6)	6.2 ± 0.9 (4.8–8.6)	0.98 (0.96–0.99)
Optic nerve sheath horizontal outer diameter (mm)	6.1 ± 0.6 (4.7–6.7)	5.7 ± 0.6 (4.7–6.3)	5.9 ± 0.6 (4.7–6.7)	0.96 (0.91–0.98)
Calculated average optic nerve diameter[b] (mm)	3.3 ± 0.4 (2.8–4.0)	2.9 ± 0.6 (1.9–4.0)	3.1 ± 0.5 (1.9–4.0)	
Calculated average subarachnoid space thickness[c] (mm)	0.9 ± 0.2 (0.5–1.1)	0.8 ± 0.1 (0.6–0.9)	0.8 ± 0.2 (0.5–1.1)	
Calculated average optic nerve sheath thickness[d] (mm)	0.5 ± 0.1 (0.4–0.7)	0.7 ± 0.2 (0.5–1.0)	0.6 ± 0.2 (0.4–1.0)	

[a]ICC and their 95% confidence intervals are given for manually marked diameters. All other diameter/thickness measurements were calculated from average horizontal and vertical diameters.

[b]Average optic nerve diameter was calculated as the mean of the horizontal and vertical optic nerve diameters.

[c]Average subarachnoid space annular thickness was calculated as half the difference between the average outer diameter of the subarachnoid space and optic nerve.

[d]Average optic nerve sheath annular thickness was calculated as half the difference between the average outer diameter of the subarachnoid space and optic nerve sheath.

through which the retinal ganglion cell axons pass (rather than the choroidal or scleral canal opening). The BMO is a consistently identifiable anatomical landmark on spectral-domain OCT[30] and remains relatively stable over time[31] compared to the clinically visible, en-face surface of the optic nerve head. We therefore used spectral-domain OCT (Spectralis OCT; Heidelberg Engineering GmbH, Heidelberg, Germany) in the same subset of participants who had ultrasound biometry (10 emmetropes, seven myopes) to determine BMO area by acquiring 24 radial B-scans (each with 768 A-scans) around the optic nerve head after determination of the fovea-BMO center axis. Each scan covered a 15° region centered on the optic disc. Scans with truncated B-scans or low quality score <30 were repeated to ensure consistent quality images. Automatic segmentation was performed by the inbuilt software to delineate the ILM and BMO points at each location (i.e., 24 radial scans). All B-scans were checked by a single experienced operator (author B.N.N.), who manually corrected the placement of the BMO point and ILM segmentation, where necessary. All OCT images had discernible BMO points. The software automatically calculated the BMO opening area (mm^2), and these data were exported for analysis.

Statistical Analysis

Statistical analysis was performed using SPSS Version 22.0. Data were tested for normality using a Kolmogorov-Smirnov test. Repeated-measures analysis of variance (ANOVA), *t*-tests, and Pearson correlational analysis were conducted for normally distributed data. Alternatively, nonparametric tests were conducted (Mann-Whitney rank sum test, Spearman rank correlational analysis) for data violating the normality rule. To evaluate the inter-rater reliability, intraclass correlation coefficients (ICC) and their 95% confidence intervals were calculated on the basis of an absolute-agreement, two-way random effects model (i.e., ICC(2, *k*)) using the mean rating of six graders ($k = 6$).[32] A P value < 0.05 was considered statistically significant.

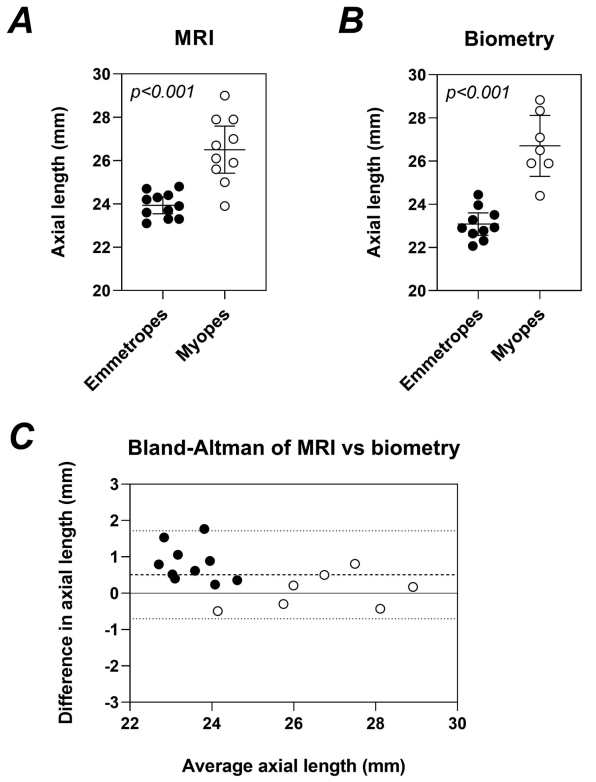

Figure 2. (**A**) Individual axial length in 11 emmetropes (*filled symbols*) and 10 myopes (*unfilled symbols*) derived from T2-weighted axial MRI images. Group mean ± 95% confidence intervals of the mean are shown. (**B**) Individual axial length in 10 emmetropes (*filled symbols*) and seven myopes (*unfilled symbols*) derived from ultrasound biometry. Group mean ± 95% confidence intervals of the mean are shown. (**C**) Bland-Altman plot, showing the difference in axial length (MRI − Biometry) as a function of average axial length derived from the two methods. The bias (average difference) was positive (0.5 mm), indicating that, on average, MRI measures of axial length were higher than those obtained by ocular biometry. The 95% limits of agreement were −0.7 to 1.7 mm. Shorter axial lengths tended to be overestimated by MRI compared to ultrasound biometry.

Results

Axial Length

Axial length of the left eye was measured along the central axis in the T2-weighted MR images, and by ultrasound biometry where possible. As expected, myopic eyes were longer than emmetropic eyes (Fig. 2A MRI: $t_{19} = 5.20$, $P < 0.001$; Fig. 2B biometry: $t_{15} = 6.56$, $P < 0.001$). MRI-derived axial length measurements were compared to those obtained by ultrasound biometry (Fig. 2C); however, the correlation between measurements was not strong. We found that MRI-derived axial length measures were, on average, greater than biometry measures (positive bias 0.5 mm), with 95% confidence limits of agreement from −0.7 to 1.7 mm. That is, in some eyes, the discrepancy between biometry and MRI-derived axial length was clinically significant (almost 2 mm in the worst case). Shorter axial lengths tended to be overestimated by MRI compared to ultrasound biometry (Fig. 2C; correlation between difference and average measurements: Spearman $r = -0.58$, $R^2 = 0.33$, $P = 0.017$).

Retrobulbar Optic Nerve, Subarachnoid Space and Optic Nerve Sheath Dimensions

Two participants' data (one emmetrope, one myope) were discarded from the analysis of the coronal oblique images because of poor image quality from excessive motion artefact, as determined by visual inspection by the radiographer, leaving data from 10 emmetropes and nine myopes. Manual placement of the first scan plane for the coronal oblique images resulted in interindividual variation in the actual distance of each participant's analyzed image behind the eyeball (range, 2–3.5 mm; emmetropes: 3.0 ± 0.4 mm; myopes: 2.8 ± 0.4 mm). However, there was no systematic difference in retrobulbar distance of the first scan plane between groups ($t_{17} = 0.63$, $P = 0.53$). Table 1 shows all retrobulbar cross-sectional area measurements (see Fig. 1E, labels a-c) averaged across the six graders, demonstrating excellent agreement (ICC > 0.90)[33] between graders.

Our cross-sectional area measurements of the optic nerve, subarachnoid space, and optic nerve sheath sum to make a total "optic nerve sheath complex."[34,35] We first determined that the cross-sectional area of the optic nerve complex did not differ between emmetropic and myopic eyes ($t_{17} = 0.80$, $P = 0.44$). Hence, any group differences in size of the constituent regions could not be attributed to an overall increase or decrease in size of the optic nerve complex as a whole. Repeated-measures ANOVA revealed a significant interaction between group and region of interest (Fig. 3A; group × region interaction: $F(2,34) = 8.00$, $P = 0.001$), which was driven by a trend for myopes to have smaller optic nerve area ($t_{17} = 1.86$, $P = 0.08$) and subarachnoid space ($t_{17} = 2.05$, $P = 0.06$) than emmetropes. However, the group difference in optic nerve sheath annular area ($t_{17} = 1.51$, $P = 0.15$) did not reach statistical significance.

Increasing MRI-derived axial length (related to the spherical equivalent refractive error; Spearman $r = -0.81$, $P < 0.0001$) was associated with smaller optic nerve area (Fig. 3B; 10 emmetropes, nine myopes: Pearson $r = -0.50$, $R^2 = 0.25$, $P = 0.03$) but not associated with the area of the subarachnoid space (Pearson $r = -0.39$, $R^2 = 0.15$, $P = 0.10$) or optic nerve sheath

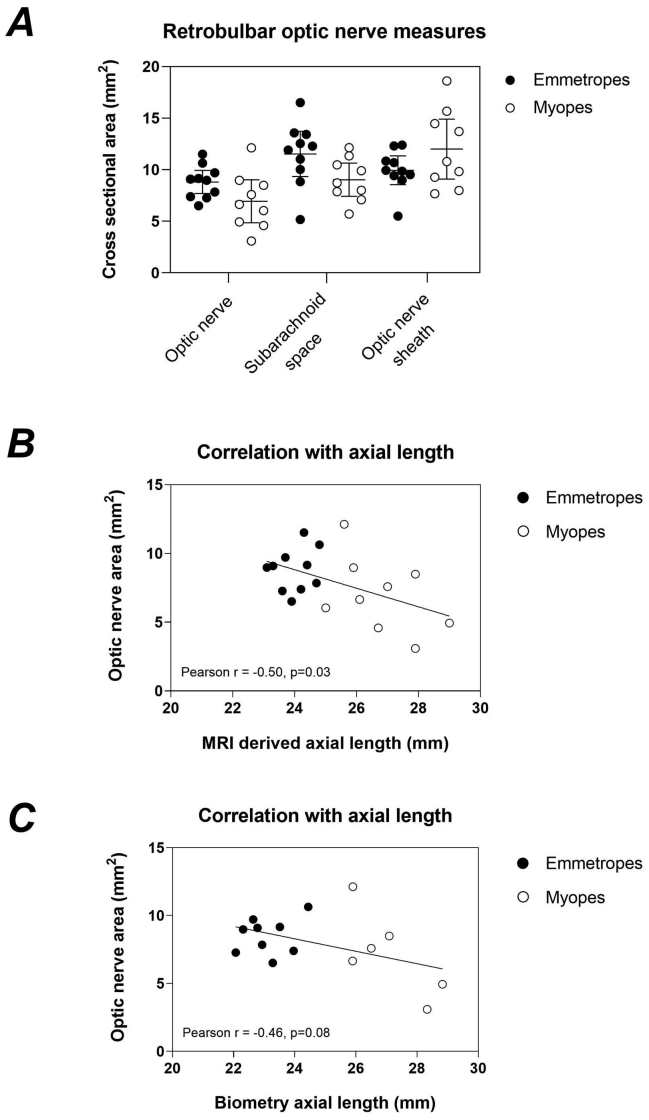

Figure 3. (**A**) Individual retrobulbar optic nerve, subarachnoid space and optic nerve sheath cross-sectional area (mm^2) in 10 emmetropes (*filled symbols*) and nine myopes (*unfilled symbols*) derived from T2-weighted axial MRI images. Group mean ± 95% confidence intervals of the mean are shown. (**B**) Correlation between MRI-derived axial length (mm) and optic nerve cross-sectional area (mm^2) in 10 emmetropes (*filled symbols*) and nine myopes (*unfilled symbols*). (**C**) Correlation between biometry axial length (mm) and optic nerve cross-sectional area (mm^2) in nine emmetropes (*filled symbols*) and six myopes (*unfilled symbols*).

(Pearson $r = 0.35$, $R^2 = 0.12$, $P = 0.14$). We also correlated retrobulbar optic nerve cross-sectional area with biometric measures of axial length. While the trend was in the same direction (increased biometry axial length was associated with smaller optic nerve area), this did not reach statistical significance, which was likely due to the smaller sample of myopic eyes with biometric measures (Fig. 3C; 9 emmetropes, 6 myopes: Pearson $r = -0.46$, $R^2 = 0.21$, $P = 0.08$).

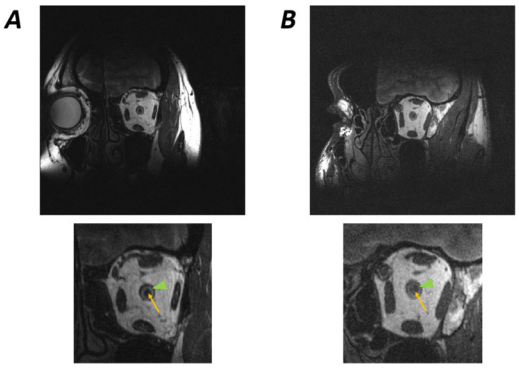

Figure 4. Example MRI cross-sectional coronal oblique images illustrating the representative group difference in subarachnoid space area. (**A**) Emmetropic left eye of a 40 year old female (0.00D spherical equivalent). (B) Myopic left eye of a 26 year old male (−6.50D spherical equivalent). In the *bottom panel* the same images have been enlarged to show the optic nerve (*orange arrow*), subarachnoid space (*green arrowhead*), and optic nerve sheath. The two eyes show the average subarachnoid space area for their respective groups, illustrating the trend in our data; that is, larger subarachnoid space area in (**A**) the emmetropic eye (11.9 mm^2) than (B) the myopic eye (8.7 mm^2), with the same total optic nerve sheath complex area (**A**) 30.7 mm^2 and (**B**) 30.9 mm^2.

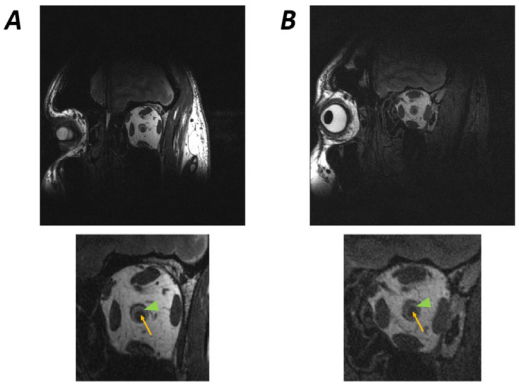

Figure 5. Example MRI cross-sectional coronal oblique images illustrating the representative group difference in optic nerve area. (**A**) Emmetropic left eye of a 23-year-old male (+0.50D spherical equivalent) (**B**) Myopic left eye of a 37-year-old male (−6.75D spherical equivalent). In the *bottom panel* the same images have been enlarged to show the optic nerve (*orange arrow*), subarachnoid space (*green arrowhead*), and optic nerve sheath. The two eyes show the average optic nerve area for their respective groups, illustrating the trend in our data; that is, larger optic nerve area in (**A**) the emmetropic eye (9.7 mm^2) than (**B**) the myopic eye (7.6 mm^2), with similar total optic nerve sheath complex area (**A**) 32.7 mm^2 and (B) 33.4 mm^2.

Figure 4 shows two representative images of the emmetropic and myopic eyes with subarachnoid space area results closest to the group mean, to illustrate the group difference in subarachnoid space. Similarly, Figure 5 shows example coronal oblique images of individual eyes that show the group mean

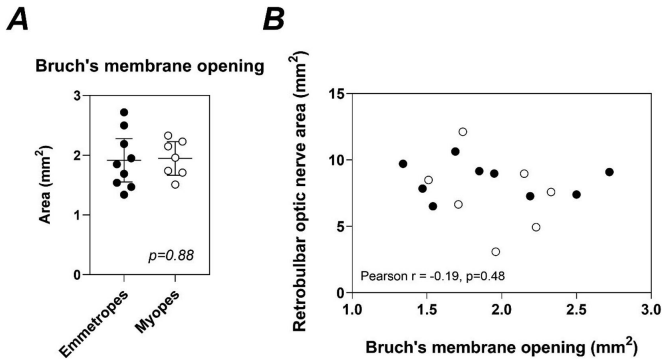

Figure 6. (**A**) Individual Bruch's membrane opening area (mm^2) in nine emmetropes (*filled symbols*) and seven myopes (*unfilled symbols*) derived from spectral-domain OCT in the subset of participants with OCT and MRI images. Group mean ± 95% confidence intervals of the mean are shown. (**B**) Correlation between OCT-derived Bruch's membrane opening area (mm^2) and MRI-derived optic nerve cross-sectional area (mm^2).

optic nerve area, illustrating the trend for reduced optic nerve size in myopes relative to emmetropes.

Table 2 has also been provided for comparison to previous morphometric data of retrobulbar optic nerve, subarachnoid space and optic nerve sheath outer diameters (see Fig. 1E, labels d–i). The group × region interaction remained significant when analyzing the optic nerve diameter, subarachnoid space thickness and optic nerve sheath thickness (see Table 2; repeated-measures ANOVA group × region interaction: $F(2,34) = 4.65$, $P = 0.02$).

Correlations Between MRI and OCT Measures

We additionally determined whether retrobulbar dimensions (from MRI) could be predicted from intraocular dimensions (from OCT). There was no difference in BMO area derived from spectral-domain OCT between myopes and emmetropes (Fig. 6A; $t_{14} = 0.15$, $P = 0.88$), and no relationship between BMO area and retrobulbar optic nerve area (Fig. 6B; Pearson $r = -0.19$, $R^2 = 0.04$, $P = 0.48$).

Discussion

This is the first study to image the retrobulbar optic nerve, subarachnoid space, and optic nerve sheath in healthy human myopic and emmetropic eyes in vivo using 7T MRI and eye coil. We were able to delineate the three regions of interest and found differences in the dimensions of the optic nerve and subarachnoid space between healthy, young myopic and emmetropic eyes. We specifically aimed to take cross-sectional MRI scans at approximately 3 mm behind the eye, as this is the region of significant clinical interest given the potential for dynamic pressure changes at this depth.[1,8–11,13,14,36] It is important to distinguish between the optic nerve, subarachnoid space and optic nerve sheath because any one or combination of these anatomical structures could contribute to a change in the overall optic nerve sheath dimensions.

To our knowledge, only one study using 3T MRI (with comparable in-plane resolution of 0.3 mm[37] compared to our 0.4 mm) has been able to demonstrate a separation between the three retrobulbar regions of interest, showing that such demarcation is possible with 3T MRI techniques if scan parameters are optimized. The majority, however, of previous T2-weighted MRI studies (1.5T and 3T) have differentiated between optic nerve and subarachnoid space (bright signal = cerebrospinal fluid, dark signal = optic nerve parenchyma) but could not visualize the thickness of the optic nerve sheath.[14,15,17,29,38–40] To address this, we manipulated several MRI variables to achieve our aim of being able to image the optic nerve, subarachnoid space, and optic nerve sheath simultaneously. We are the first to use 7T MRI to image the retrobulbar optic nerve in cross-section. 7T imaging produces higher SNR than comparable 3T imaging, because of the approximately linear relationship between SNR and magnetic field strength.[41] The use of a multichannel surface coil (with each coil being small and placed close enough to the eye to provide sufficient radiofrequency depth penetration[20]) to image our region of interest takes full advantage of the signal that can be obtained at 7T. This improvement in SNR allows for increased resolution within acceptable imaging times (<3 minutes). The achievable thinner slices (0.7 mm compared to 2 mm[37]) from theoretically increased resolution reduce the well-known "partial volume artefact" seen in all MRI imaging. Slices create a partial volume effect, or imprecisely defined voxels containing fractional amounts of signal from overlapping of adjacent tissues. As the resultant MRI signal is a weighted average of signals from different structures, the thickness of the slice then determines how much anatomy "blurring" occurs and how feasible it is to delineate a particular structure; in our case, we were able to differentiate between different anatomical structures with 0.4 mm resolution. Further improvements could possibly be made to our initial scan protocol, such as narrowing the field of view (to improve spatial resolution) and shortening acquisition times or adopting novel motion-resolved image reconstruction methods[42] to reduce the inevitable confound of motion artefact in eye imaging.

A key technical point arising from this study for consideration in future MRI work, especially given the recruitment of highly myopic participants, is the use of an appropriate fixation task. Our fixation target was customized in size for each participant's visual acuity (i.e., larger for higher myopes) and therefore sufficiently small to control for large eye movements. The interactive button pressing also helped to maintain attention throughout the scanning. We have recently shown that the use of such a fixation task, in conjunction with the imaged eye being taped closed, prevents significant motion artefact and is tolerated well by all participants.[43]

Although we presented dimensions primarily in terms of cross-sectional area (Table 1), we have also included the thickness/diameter of the optic nerve, subarachnoid space, and outer optic nerve sheath in Table 2 to enable comparison with previous literature. We are only aware of one article that presents dimensions of the three retrobulbar regions of interest here (optic nerve, subarachnoid space and optic nerve sheath diameter).[37] Although that study encompassed a wider and older age range (38 ± 18 years) of healthy control participants, we find remarkably similar measures of optic nerve sheath diameter (6.1 ± 0.6 mm in the present study versus 6.2 ± 0.5 mm),[37] suggesting that optic nerve sheath diameter remains consistent across a lifespan in healthy, nonmyopic eyes. Thus, MRI measures of optic nerve sheath diameter could serve as a stable baseline for monitoring structural change in clinical settings. More work is required, however, to obtain normative data for optic nerve sheath diameter across a wide age range and in a larger sample population, given the potential for significant interindividual variation in sheath elasticity[5] and mediation of tissue composition by matrix metalloproteinases[44] that likely contribute to optic nerve sheath diameter.

Our control cohort showed smaller optic nerve diameter and optic nerve sheath thickness (6% and 28% relative reduction, respectively) but larger subarachnoid space (33% relative increase) compared to a previous study.[37] These differences could be an artefact of methodological variation. For example, we measured at approximately 3 mm behind the eyeball, but, given the normal decrease in optic nerve diameter[45] and optic nerve sheath diameter[1] along its intraorbital length, it is possible that previous MRI work focused on a portion of the optic nerve closer to the eyeball (retrobulbar distance not reported by Demer[37]). It is therefore important for normative data to be obtained at the same retrobulbar location, preferably at 3 mm behind the eyeball where diameters are physiologically largest (hence, low relative measurement error) and where sensitivity to detect a pressure-related change in size is highest. Age or some other demographic factor could also contribute to differences in dimensions; however, because of the small number of participants in our study, we are unable to comment on the possible contribution of these factors.

A scarcely reported finding is the thickness of the optic nerve sheath itself, which, according to histological studies, does not appear to change along its intraorbital trajectory.[1] Mashima and colleagues[15] surmised that the optic nerve sheath could not be well visualized in their 1.5T MRI study because of resolution constraints (3 mm slice thickness, 0.9 mm in-plane resolution) and interference from chemical shift artefact. With improved in-plane resolution (0.3–0.4 mm in-plane resolution), we found an average in vivo optic nerve sheath thickness of 0.5 mm (± 0.1 mm), respectively, which is larger than reported from postmortem eyes (average 0.4 mm, range, 0.35 to 0.5 mm).[1,2] Whether this measurement discrepancy relates to the preparation of postmortem eyes is open to debate.

In this study, we did not conduct ultrasound imaging of the retrobulbar optic nerve. Although the focus of this study was on MRI techniques to image the optic nerve, subarachnoid space, and optic nerve sheath simultaneously, we do acknowledge that ultrasonography can also be used to differentiate between regions of interest according to how hyperechogenic or hypoechogenic the signal is. The optic nerve is hypoechogenic, and its diameter can typically be reliably determined (distance between the inner edges of the hyperechogenic pia mater), whereas the optic nerve sheath diameter has been taken as the distance between the inner edges of the hyperechogenic dura mater.[12,46] These two measures are most commonly reported in ultrasonographic studies of the retrobulbar optic nerve; however, the surrounding orbital fat can also appear as hyperechogenic as the dura mater, making it difficult to discern the outermost border of the optic nerve sheath and therefore not as readily comparable to our MRI-derived measures. Although subarachnoid space can also be seen as two hypoechogenic bands around the optic nerve on high-resolution ultrasound systems,[46] many studies have not specifically measured subarachnoid space until more recently.[47] It would be worthwhile comparing measures obtained by both high-resolution ultrasonography and ultra–high field MRI to determine clinically useful normative measures of retrobulbar anatomy. Nevertheless, relative to ultrasonography, the clinical utility of 7T MRI-derived normative data is especially promising given that ex vivo measurements of optic nerve sheath diameter in

porcine eyes better match 7T MRI than ultrasound measures.[48]

Although changes in optic nerve sheath diameter are used clinically as a proxy for raised intracranial pressure, there is conjecture in the literature regarding the degree of correlation[49] and its sensitivity and specificity.[50] Moreover, there is a pervasive assumption that increased optic nerve sheath diameter must be due to an expansion of the subarachnoid space. However, it is yet to be determined whether pressure-related enlargement of optic nerve sheath diameter is associated with any change in the thickness of the optic nerve sheath itself (not reported by Hansen and Helmke,[1] for example). Future work in clinical populations could use 7T MRI, as demonstrated here, to measure the effect of raised intracranial pressure on optic nerve sheath and subarachnoid space (thickness and diameter), and not just optic nerve sheath diameter.

Morphometric studies of retrobulbar anatomy almost exclusively report "diameter" as the average of horizontal and vertical diameter measurements, assuming that the optic nerve and surrounding anatomy is circular and symmetric. Although we were careful to plan each scan according to each individual's anatomy, slight tilting of the coronal oblique scan plane may have resulted in an elliptical representation of the optic nerve. For this reason, we chose not to assume circular asymmetry and reported cross-sectional area as the main outcome measures of interest instead, to account for any departure from circular geometry. In the future, one way to minimize the effect of small angle deviations might be to expand 2D models of eye geometry to create 3D volumetric measures (see preliminary work by Wasi and Moss[51]), although such an approach is likely to be difficult for measuring subarachnoid space more posteriorly because of the progressive decrease in size of the optic nerve and outer sheath diameter (hence, smaller fluid gap in between) along the intraorbital trajectory.[1,45]

We also demonstrated that retrobulbar optic nerve size cannot be predicted from the BMO size, which highlights the importance of imaging techniques that are able to penetrate past the eyeball. We chose to characterize BMO using spectral-domain OCT because it is a stable and identifiable landmark.[30] Although larger BMOs are correlated with longer axial length, particularly for axial lengths greater than 26 mm,[52] the BMO detected using spectral-domain OCT is not the same as the clinically visible optic disc margin.[30] Moreover, Winder and Atta[53] used ultrasonography to measure "sheath-to-sheath" retrobulbar optic nerve dimensions in a range of eyes (healthy, glaucomatous, hypoplastic, ocular hypertensive) and did not find a correlation between neuroretinal rim size (intraocularly) and the presumed width of the retrobulbar optic nerve. These findings, including ours, suggest that the increase in size of the optic nerve in the retrobulbar "bulbous" region (approximately 3 mm behind the eyeball) cannot be predicted from intraocular measures.

We chose to study both emmetropic and nonpathological myopic eyes, because myopia is a risk factor for glaucoma.[23] Participants were enrolled on the basis of their refractive error and not their axial length; nevertheless, we were able to verify that MRI and biometry measures of axial length were correlated to refractive error (spherical equivalent), as expected. It is not entirely clear why we find, in some cases, a clinically significant discrepancy between our two measures of axial length. Recently, Franceschiello and colleagues[42] report an absolute difference in MRI and biometric axial length measurements of 0.5 mm, the same magnitude of bias found here. However, given that we measured MRI axial length from the posterior rather than anterior surface of the cornea, one would expect a negative bias (i.e., MRI estimates lower than biometric estimates of axial length),[54] rather than the positive bias found here. Furthermore, the ultrasound biometer used in this study measures axial length to the ILM layer of the retina; such precision is not possible in our T2-weighted MR images (the main contrast is the edge of the water-rich vitreous) and cannot explain the overestimation of axial length by MRI. In particular, we found that MRI tended to overestimate axial length in shorter eyes, compared to ultrasound biometry. This has also been reported in a study comparing 7T MRI-derived measures of lens-retina distance to partial coherence interferometry, an alternative optical method of biometry.[55]

We found a relationship between cross-sectional area and axial length, which is unlikely to be an artefact of decreasing sensitivity of the eye coil with increasing distance. The contrast-to-noise ratio (contrast resolution) of our 7T scans was approximately 20:1, which is four times the Rose criteria cutoff of 5:1[56] for image features to be distinguished reliably. There would need to be at least an average of 50% signal-to-noise drop to impact significantly on contrast-to-noise ratio, which we consider unlikely comparing the emmetropic and myopic coronal oblique scans. Although the precise reasons for the association between glaucomatous optic neuropathy and myopia are yet to be fully elucidated, there is increasing evidence of posterior structural differences in myopic eyes[25] that could contribute to increased susceptibility to optic nerve damage. Histomorphometric studies of enucleated highly myopic eyes (axial length >26.5 mm) show

decreased lamina cribrosa thickness, which is thought to reduce the ability to resist deformation and alter the pressure gradient between intraocular and intracranial pressure at the point of optic nerve insertion.[57] Highly axial myopic eyes also have a thinner scleral flange,[24] which effectively increases the optic nerve area exposed to cerebrospinal fluid pressure in the abutting subarachnoid space. Furthermore, the subarachnoid space is extended into the immediate retroparapapillary region in highly myopic eyes (at an image depth plane of approximately 2 mm posterior to the lamina cribrosa).[24] These structural changes are visible as a triangular void on swept-source OCT (but otherwise invisible in emmetropic eyes)[58,59] and presumably alter the hydrodynamics of cerebrospinal fluid in the retrobulbar region. Thus the literature to date implies that axial elongation is associated with a redistribution of subarachnoid space (and by extension, a redistribution of cerebrospinal fluid).[24,58,59] We hypothesize that with increasing axial length, the reduction in subarachnoid space (seen cross-sectionally at approximately 3 mm behind the eyeball) is a result of fluid being "squeezed" more anteriorly into the immediate retroparapapillary region (as seen by other studies using swept-source OCT[58,59]), but this proposed association will require future confirmation in a larger, highly myopic cohort.

In summary, we have successfully demonstrated feasibility of using ultra-high field MRI to delineate three retrobulbar anatomical regions of interest: the optic nerve, subarachnoid space, and optic nerve sheath. In healthy eyes, the cross-sectional dimensions of the optic nerve and subarachnoid space at approximately 3 mm behind the eyeball are influenced by degree of myopia. This study paves the way for a novel body of work utilizing advanced imaging techniques to comprehensively characterize the retrobulbar optic nerve and surrounding structures in vivo in people with and without ocular pathologies.

Acknowledgments

The authors thank the assistance of Juan Sepulveda for part of the data collection.

Supported by a Melbourne Neuroscience Institute Fellowship (B.N.N.), The University of Melbourne McKenzie Fellowship (J.O.C.), a Melbourne Neuroscience Institute Interdisciplinary Seed Funding Grant (A.M.M., B.V.B., R.J.O.), and a National Imaging Fellowship (B.A.M.). The 7T system at the Melbourne Brain Centre Imaging Unit is supported by the Australian National Imaging Facility via the Australian Government's National Collaborative Research Infrastructure Strategy program.

Disclosure: **B.N. Nguyen,** None; **J.O. Cleary,** None; **R. Glarin,** None; **S.C. Kolbe,** None; **B.A. Moffat,** None; **R.J. Ordidge,** None; **B.V. Bui,** None; **A.M. McKendrick,** None

References

1. Hansen HC, Helmke K. The subarachnoid space surrounding the optic nerves. An ultrasound study of the optic nerve sheath. *Surg Radiol Anat*. 1996;18:323–328.
2. Liu D, Kahn M. Measurement and relationship of subarachnoid pressure of the optic nerve to intracranial pressures in fresh cadavers. *Am J Ophthalmol*. 1993;116:548–556.
3. Anderson DR. Fine structure and function of ocular tissues. The optic nerve. *Int Ophthalmol Clin*. 1973;13:229–242.
4. Anderson DR, Hoyt WF. Ultrastructure of intraorbital portion of human and monkey optic nerve. *Arch Ophthalmol*. 1969;82:506–530.
5. Hansen HC, Helmke K. Validation of the optic nerve sheath response to changing cerebrospinal fluid pressure: ultrasound findings during intrathecal infusion tests. *J Neurosurg*. 1997;87:34–40.
6. Helmke K, Hansen HC. Fundamentals of transorbital sonographic evaluation of optic nerve sheath expansion under intracranial hypertension II. Patient study. *Pediatr Radiol*. 1996;26:706–710.
7. Helmke K, Hansen HC. Fundamentals of transorbital sonographic evaluation of optic nerve sheath expansion under intracranial hypertension. I. Experimental study. *Pediatr Radiol*. 1996;26:701–705.
8. Hansen HC, Helmke K, Kunze K. Optic nerve sheath enlargement in acute intracranial hypertension. *Neuro-Ophthalmology*. 1994;14:345–354.
9. Brodsky MC, Vaphiades M. Magnetic resonance imaging in pseudotumor cerebri. *Ophthalmology*. 1998;105:1686–1693.
10. Zaidi SJ, Yamamoto LG. Optic nerve sheath diameter measurements by CT scan in ventriculoperitoneal shunt obstruction. *Hawaii J Med Public Health*. 2014;73:251–255.
11. Geeraerts T, Newcombe VF, Coles JP, et al. Use of T2-weighted magnetic resonance imaging of the optic nerve sheath to detect raised intracranial pressure. *Crit Care*. 2008;12:R114.

12. Geeraerts T, Merceron S, Benhamou D, Vigue B, Duranteau J. Non-invasive assessment of intracranial pressure using ocular sonography in neurocritical care patients. *Intensive Care Med*. 2008;34:2062–2067.
13. Rohr A, Jensen U, Riedel C, et al. MR imaging of the optic nerve sheath in patients with craniospinal hypotension. *AJNR Am J Neuroradiol*. 2010;31:1752–1757.
14. Watanabe A, Kinouchi H, Horikoshi T, Uchida M, Ishigame K. Effect of intracranial pressure on the diameter of the optic nerve sheath. *J Neurosurg*. 2008;109:255–258.
15. Mashima Y, Oshitari K, Imamura Y, Momoshima S, Shiga H, Oguchi Y. High-resolution magnetic resonance imaging of the intraorbital optic nerve and subarachnoid space in patients with papilledema and optic atrophy. *Arch Ophthalmol*. 1996;114:1197–1203.
16. Pache M, Meyer P. Morphological changes of the retrobulbar optic nerve and its meningeal sheaths in glaucoma. *Ophthalmologica*. 2006;220:393–396.
17. Lagreze WA, Lazzaro A, Weigel M, Hansen HC, Hennig J, Bley TA. Morphometry of the retrobulbar human optic nerve: comparison between conventional sonography and ultrafast magnetic resonance sequences. *Invest Ophthalmol Vis Sci*. 2007;48:1913–1917.
18. Steinborn M, Fiegler J, Kraus V, et al. High resolution ultrasound and magnetic resonance imaging of the optic nerve and the optic nerve sheath: anatomic correlation and clinical importance. *Ultraschall Med*. 2011;32:608–613.
19. Beenakker JW, van Rijn GA, Luyten GP, Webb AG. High-resolution MRI of uveal melanoma using a microcoil phased array at 7 T. *NMR Biomed*. 2013;26:1864–1869.
20. Graessl A, Muhle M, Schwerter M, et al. Ophthalmic magnetic resonance imaging at 7 T using a 6-channel transceiver radiofrequency coil array in healthy subjects and patients with intraocular masses. *Invest Radiol*. 2014;49:260–270.
21. Richdale K, Wassenaar P, Teal Bluestein K, et al. 7 Tesla MR imaging of the human eye in vivo. *J Magn Reson Imaging*. 2009;30:924–932.
22. Christoforidis JB, Wassenaar PA, Christoforidis GA, Ho VY, Knopp MV, Schmalbrock PM. Retrobulbar vasculature using 7-T magnetic resonance imaging with dedicated eye surface coil. *Graefes Arch Clin Exp Ophthalmol*. 2013;251:271–277.
23. Marcus MW, de Vries MM, Junoy Montolio FG, Jansonius NM. Myopia as a risk factor for open-angle glaucoma: a systematic review and meta-analysis. *Ophthalmology*. 2011;118:1989–1994 e1982.
24. Jonas JB, Jonas SB, Jonas RA, Holbach L, Panda-Jonas S. Histology of the parapapillary region in high myopia. *Am J Ophthalmol*. 2011;152:1021–1029.
25. Jonas JB, Xu L. Histological changes of high axial myopia. *Eye*. 2014;28:113–117.
26. Ohno-Matsui K, Lai TY, Lai CC, Cheung CM. Updates of pathologic myopia. *Prog Retin Eye Res*. 2016;52:156–187.
27. Bert RJ, Patz S, Ossiani M, et al. High-resolution MR imaging of the human eye 2005. *Acad Radiol*. 2006;13:368–378.
28. Schmidt P, Kempin R, Langner S, et al. Association of anthropometric markers with globe position: A population-based MRI study. *PloS One*. 2019;14:e0211817.
29. Xie X, Chen W, Li Z, et al. Noninvasive evaluation of cerebrospinal fluid pressure in ocular hypertension: a preliminary study. *Acta Ophthalmol*. 2018;96:e570–e576.
30. Chauhan BC, Burgoyne CF. From clinical examination of the optic disc to clinical assessment of the optic nerve head: a paradigm change. *Am J Ophthalmol*. 2013;156:218–227.e212.
31. Belghith A, Bowd C, Medeiros FA, et al. Does the Location of Bruch's Membrane Opening Change Over Time? Longitudinal Analysis Using San Diego Automated Layer Segmentation Algorithm (SALSA). *Invest Ophthalmol Vis Sci*. 2016;57:675–682.
32. Shrout PE, Fleiss JL. Intraclass correlations: uses in assessing rater reliability. *Psychol Bull*. 1979;86:420–428.
33. Koo TK, Li MY. A guideline of selecting and reporting intraclass correlation coefficients for reliability research. *J Chiropr Med*. 2016;15:155–163.
34. Ozgen A, Aydingoz U. Normative measurements of orbital structures using MRI. *J Comput Assist Tomogr*. 2000;24:493–496.
35. Shen S, Fong KS, Wong HB, et al. Normative measurements of the Chinese extraocular musculature by high-field magnetic resonance imaging. *Invest Ophthalmol Vis Sci*. 2010;51:631–636.
36. Hansen HC, Lagreze W, Krueger O, Helmke K. Dependence of the optic nerve sheath diameter on acutely applied subarachnoidal pressure - an experimental ultrasound study. *Acta Ophthalmol*. 2011;89:e528–532.
37. Demer JL. Optic nerve sheath as a novel mechanical load on the globe in ocular duction. *Invest Ophthalmol Vis Sci*. 2016;57:1826–1838.

38. Lam BL, Glasier CM, Feuer WJ. Subarachnoid fluid of the optic nerve in normal adults. *Ophthalmology*. 1997;104:1629–1633.
39. Weigel M, Lagreze WA, Lazzaro A, Hennig J, Bley TA. Fast and quantitative high-resolution magnetic resonance imaging of the optic nerve at 3.0 tesla. *Invest Radiol*. 2006;41:83–86.
40. Harrigan RL, Plassard AJ, Bryan FW, et al. Disambiguating the optic nerve from the surrounding cerebrospinal fluid: Application to MS-related atrophy. *Magn Reson Med*. 2016;75:414–422.
41. Brown RW, Cheng YN, Haacke EM, Thompson MR, Venkatesan R. *Magnetic resonance imaging: Physical principles and sequence design* (2nd ed). Hoboken, NJ: Wiley-Blackwell; 2014.
42. Franceschiello B, Di Sopra L, Minier A, et al. 3-Dimensional magnetic resonance imaging of the freely moving human eye. *Prog Neurobiol*. 2020;194:101885.
43. Glarin R, Nguyen BN, Cleary JO, et al. MR-EYE: High resolution magnetic resonance imaging of the human eye and orbit at ultrahigh field (7T). *Magn Reson Imaging Clin N Am*. 2021;29:103–116.
44. Jaggi GP, Miller NR, Flammer J, Weinreb RN, Remonda L, Killer HE. Optic nerve sheath diameter in normal-tension glaucoma patients. *Br J Ophthalmol*. 2012;96:53–56.
45. Karim S, Clark RA, Poukens V, Demer JL. Demonstration of systematic variation in human intraorbital optic nerve size by quantitative magnetic resonance imaging and histology. *Invest Ophthalmol Vis Sci*. 2004;45:1047–1051.
46. Topcuoglu MA, Arsava EM, Bas DF, Kozak HH. Transorbital Ultrasonographic Measurement of Optic Nerve Sheath Diameter in Brain Death. *J Neuroimaging*. 2015;25:906–909.
47. Cennamo G, Montorio D, Breve MA, Brescia Morra V, Menna F, Cennamo G. Evaluation of optic nerve subarachnoid space in primary open angle glaucoma using ultrasound examination. *PloS One*. 2018;13:e0208064.
48. Nusbaum DM, Antonsen E, Bockhorst KH, et al. Optic nerve sheath diameter measurement techniques: examination using a novel ex-vivo porcine model. *Aviat Space Environ Med*. 2014;85:50–54.
49. Pircher A, Montali M, Berberat J, Remonda L, Killer HE. Relationship between the optic nerve sheath diameter and lumbar cerebrospinal fluid pressure in patients with normal tension glaucoma. *Eye*. 2017;31:1365–1372.
50. Le A, Hoehn ME, Smith ME, Spentzas T, Schlappy D, Pershad J. Bedside sonographic measurement of optic nerve sheath diameter as a predictor of increased intracranial pressure in children. *Ann Emerg Med*. 2009;53:785–791.
51. Wasi M, Moss H. Patient specific models of eye geometry in high intracranial pressure states based on magnetic resonance images. *Invest Ophthalmol Vis Sci*. 2019;60:3599–3599.
52. Zhang Q, Xu L, Wei WB, Wang YX, Jonas JB. Size and shape of Bruch's membrane opening in relationship to axial length, gamma zone, and macular Bruch's membrane defects. *Invest Ophthalmol Vis Sci*. 2019;60:2591–2598.
53. Winder S, Atta HR. Ultrasonography of the optic disc cup in discs of various sizes. *Eye*. 1996;10(Pt 6):732–736.
54. Tang J, Pan JY, Chang S, Hoang QV. Comparison of ocular axial length measurements with MRI and partial coherence interferometry in highly myopic patients with posterior staphyloma. *Invest Ophthalmol Vis Sci*. 2014;55:5939.
55. Beenakker JW, Shamonin DP, Webb AG, Luyten GP, Stoel BC. Automated retinal topographic maps measured with magnetic resonance imaging. *Invest Ophthalmol Vis Sci*. 2015;56:1033–1039.
56. Watts R, Wang Y. k-space interpretation of the Rose model: noise limitation on the detectable resolution in MRI. *Magn Reson Med*. 2002;48:550–554.
57. Jonas JB, Berenshtein E, Holbach L. Lamina cribrosa thickness and spatial relationships between intraocular space and cerebrospinal fluid space in highly myopic eyes. *Invest Ophthalmol Vis Sci*. 2004;45:2660–2665.
58. Fan H, Ma H, Gao R, et al. Associated factors for visibility and width of retrobulbar subarachnoid space on swept-source optical coherence tomography in high myopia. *Sci Rep*. 2016;6:36723.
59. Ohno-Matsui K, Akiba M, Moriyama M, Ishibashi T, Tokoro T, Spaide RF. Imaging retrobulbar subarachnoid space around optic nerve by swept-source optical coherence tomography in eyes with pathologic myopia. *Invest Ophthalmol Vis Sci*. 2011;52:9644–9650.